Minimization of diffraction peaks of spatial light modulators using Voronoi diagrams

Céline Benoit-Pasanau, François Goudail, Pierre Chavel, Jean-Paul Cano, Jérôme Ballet

Minimization of diffraction peaks of spatial light modulators using Voronoi diagrams

Céline Benoît-Pasanau,[1,2] François Goudail,[1,*] Pierre Chavel,[1]
Jean-Paul Cano,[2] and Jérôme Ballet[2]

[1]*Laboratoire Charles Fabry de l'Institut d'Optique, CNRS, Univ Paris-Sud, Campus Polytechnique, RD 128, 91127 Palaiseau, France*
[2]*Essilor International, Rue Pierre et Marie Curie, 31670 Labège, France*
*[*francois.goudail@institutoptique.fr](mailto:francois.goudail@institutoptique.fr)*

Abstract: It is possible to reduce the diffraction peaks of a Spatial Light Modulator (SLM) by breaking the periodicity of the pixels shape. We propose a theoretical investigation of a SLM that would be based on a Voronoi diagram, obtained by deforming a regular grid, and show that for a specific deformation parameter the diffraction peaks disappear and are replaced with a speckle-like diffraction halo. We also develop a simple model to determine the shape and the level of this halo.

© 2010 Optical Society of America

OCIS codes: (050.1940) Diffraction; (230.6120) Spatial light modulators.

References and links

1. S.-W. Chung and Y.-K. Kim, "Design and fabrication of 10×10 micro-spatial light modulator array for phase and amplitude modulation," Sens. Actuators A **78**(1), 63–70 (1999).
2. J. M. Younse, "Mirrors on a chip," IEEE Spectrum **30**(11), 27–31 (1993).
3. J. M. Younse, "Projection display systems based on the digital micromirror device (DMD)," Proc. SPIE **2641**, 64–75 (1995).
4. L. J. Hornbeck, "Deformable mirror spatial light modulator," Spat. Light Modulators Appl. 3 SPIE Crit. Rev. **1150**, 86–102 (1990).
5. R. B. Apte, F. S. A. Sandejas, W. C. Banyai, and D. M. Bloom, "Deformable grating light valves for high resolution displays," Solid-State Sensor and Actuator Workshop, Hilton-Head, SC, 1–6 (1994).
6. S. H. Lee, S. L. Lee, and H. Y. Kim, "Electro-optic characteristics and switching principle of a nematic liquid crystal cell controlled by fringe-field switching," Appl. Phys. Lett. **73**, 2881–2883 (1998).
7. G. D. Love, "Wave-front correction and production of Zernike modes with a liquid-crystal spatial light modulator," Appl. Opt. **36**(7), 1517–1524 (1997).
8. D. M. Cottrell, J. A. Davis, T. R. Hedman, and R. A. Lilly, "Multiple imaging phase-encoded optical elements written as programmable spatial light modulators," Appl. Opt. **29**(17), 2505–2509 (1990).
9. W-H. Lee, "Computer-Generated Holograms: Techniques and Applications," Prog. Opt. **16**, 119–232 (1978).
10. G. F. Voronoi, "Nouvelles applications des paramètres continus à la théorie des formes quadratiques," J. Reine Angew. Math. **134**, 198–287 (1908).

1. Introduction

Spatial Light Modulators (SLMs) are components that can locally modulate the amplitude and / or the phase of an incoming wavefront [1]. One can cite DMD (Deformable Micromirror Device) [2–5] and nematic liquid crystals [6,7] as representative examples. Here, we shall consider transmissive SLMs, although the concepts apply equally well to reflective devices. SLMs are

often pixellated, that is, divided in small cells whose transmittance is constant and that are separated by walls. The pixels are in general square or rectangle-shaped and distributed periodically over the plane of the modulator. Due to that periodic arrangement, the images formed by such devices are often affected by artifacts that can bother a human observer or perturb automatic analysis of the images [8]. We shall consider more specifically SLMs used in the Fraunhofer diffraction regime, where the intensity distribution of interest to the observer is the squared modulus of the Fourier transform of the SLM complex amplitude transmittance. In that case, unwanted, periodically distributed diffraction peaks arise in the observation plane. As one typical example, the situation occurs for the display of a complex amplitude distribution obtained by computer generated holography [9]. Please note however that the specific complex amplitude distribution displayed on the SLM is not our concern here, and we are solely interested in the effect of the pixel shape. In our analysis, we shall therefore assume that the transmittances of all the pixels of the SLM are the same and concentrate on the Fraunhofer diffraction pattern that results from the pixels shape.

To reduce the diffraction peaks, it is attractive to break the periodicity by employing other spatial distributions of pixel shapes and sizes. The purpose of this article is to propose ways of designing such distributions by starting from a regular square shape grid and deforming it with the technique of Voronoi diagrams [10]. In particular, we will determine the deformation parameters that minimize the diffractions peaks. It should be stressed that we shall focus on the optimization of the structure of the modulators and we shall not address their fabrication or their electrical addressing issues.

In Section 2, we shall briefly describe our design technique and show that the deformation of the modulator grid induces a reduction of the diffraction peaks and the apparition of a speckle-like diffraction halo around the zero-order peak. In Section 3, we shall develop a simple model to determine the shape and the level of the diffraction halo. In Section 4, we shall model the evolution of the diffraction peaks and identify values of the deformation parameter for which they completely disappear. We shall then conclude and give perspectives for this work.

2. Description of the problem

Let us start from a structure where the walls that separate the cells form a square grid. The centres of the cells also lie on a square grid with the same periodicity that we denote d. In order to introduce disorder in the structure, we randomly displace the cell centres according to a given statistical law. One can associate to each new cell centre p_i its Voronoi cell, which is the set of all the points that are closer to p_i than to any other centre p_j ($j \neq i$). The set of all the Voronoi cells is called a Voronoi diagram, as it is shown on Fig. 1. The new grid structure is defined as the Voronoi diagram obtained from the displaced cell centres. For example, we have represented on Fig. 2, different grid structures that correspond to different levels of disorder. They have been generated by displacing the cell centres so that each displacement in x and y direction is the realization of a uniform random variable in the interval $[-\alpha/2, \alpha/2]$. We define the deformation factor as follows :

$$a = \frac{\alpha}{d} \tag{1}$$

The grids in Fig. 2 correspond to different values of a. We have also represented in this figure the histograms of wall orientations of each grid. The most interesting characteristic of these structures is the way in which they affect the quality of the image of a point-like object when the SLM is placed in the pupil of the imaging system. For that purpose, we have assumed that the modulator is placed in the pupil of a perfect lens and illuminated by a monochromatic plane wave of wavelength λ, propagating parallel to the optical axis. We observe the distribution of light intensity in the focal plane, which is, in this simple case, the squared modulus of the
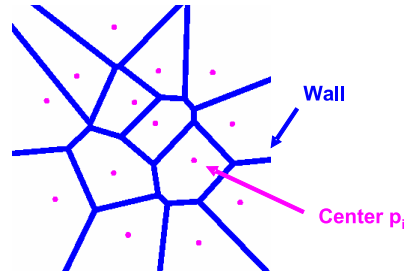
Fig. 1. Voronoi diagram

Fourier transform of the modulator transmittance. For simplicity's sake, we assume that the walls are absorbing (transmittance equal to 0) and the cells are transparent (transmittance equal to 1). The walls thickness is $e = d/20$ and the modulator aperture is a disc of diameter $2R$. We have represented in Fig. 3 the two dimensional intensity distribution in the focal plane for each modulator shape represented in Fig. 2 as well as a cross section in the horizontal direction. Here and in the following, the conditions of scalar, low angle approximations are assumed to be valid.

In Fig. 2a, the grid is square shaped with pixel pitch equal to d, in this case with $d = R/20$. There are only two possible wall orientations, as appears clearly in the histogram in Fig. 2b. Its is observed in Fig. 3a and 3b that the intensity distribution in the focal plane consists of a zeroth order, located at zero diffraction angle (highlighted by a circle on Fig. 3) and of secondary orders (peaks) periodically distributed with an angular period equal to λ/d. For example, the first order peak is highlighted by a dotted circle on Fig. 3b.

The grid structure represented in Fig. 2c corresponds to a small deformation of the square grid with a parameter $a = 0.5$. It is seen in Fig. 2d that the orientations of the walls are more scattered than in the regular case but the walls still possess privileged orientations. It is also observed in Fig. 3c and 3d that the amplitudes of the higher order peaks are reduced, especially those located at angles larger than $3\lambda/d$. On the other hand, a scattered light distribution appears between the peaks. In the following, we shall call it the diffraction "halo".

The grid structure represented in Fig. 2e corresponds to a larger deformation factor ($a = 1.27$) : it is seen on Fig. 2f that the orientations of the walls are quasi-uniformly distributed over $[0, \pi]$. Indeed, the estimated variance of the wall orientation angle expressed in radian is $\sigma^2 = 0.826$, which is quite close to the value corresponding to a uniform distribution over $[0, \pi]$, i.e $\pi^2/12 = 0.82$. If we look at the intensity distribution in Fig. 3e and 3f, all the higher order peaks have disappeared and the level of the halo has slightly increased. If a is further increased, as in Fig. 2g ($a = 1.5$), we see in Fig. 2h that wall orientations remain uniformly distributed but the first and second diffraction peaks slightly reappear (see Fig. 3g and 3h).

This example shows that increasing the deformation factor generates two phenomena. Firstly, the higher order peaks diminish, disappear and then slightly reappear. Secondly, the energy of the diffraction peaks is transferred to a speckle-like halo. Our purpose in the sequel of this paper will be to explain these phenomena using simple heuristic models. In Section 3, we will propose a model for the halo, and in Section 4, we will explain the evolution of the higher order peak intensities as the deformation factor varies.
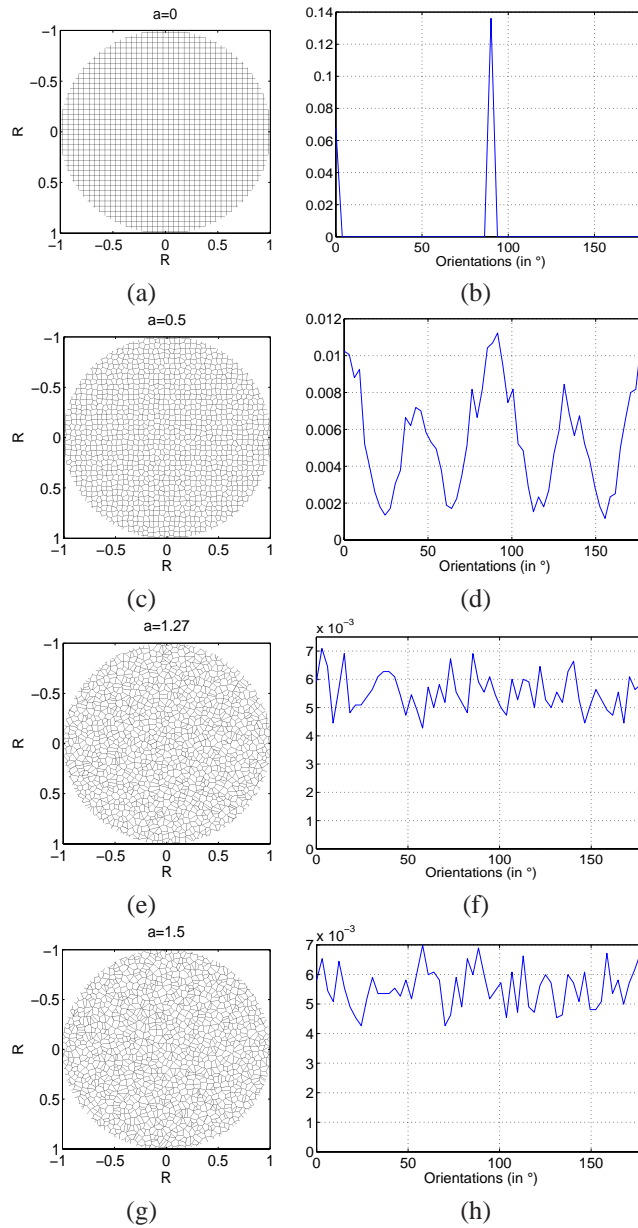
Fig. 2. Effect of an increasing randomness in the distribution of the cell centres. The initial square grid (a) has a pitch equal to $d = 100\mu m$. Pupil radius $R = 2mm$. (c, e, g) : Associated Voronoi diagrams. The centres are moved according to a uniform distribution on a square of side $\alpha = ad$ with $a = 0.5$, $a = 1.27$ and $a = 1.5$. (b, d, f, h) : Corresponding histograms of wall orientations.
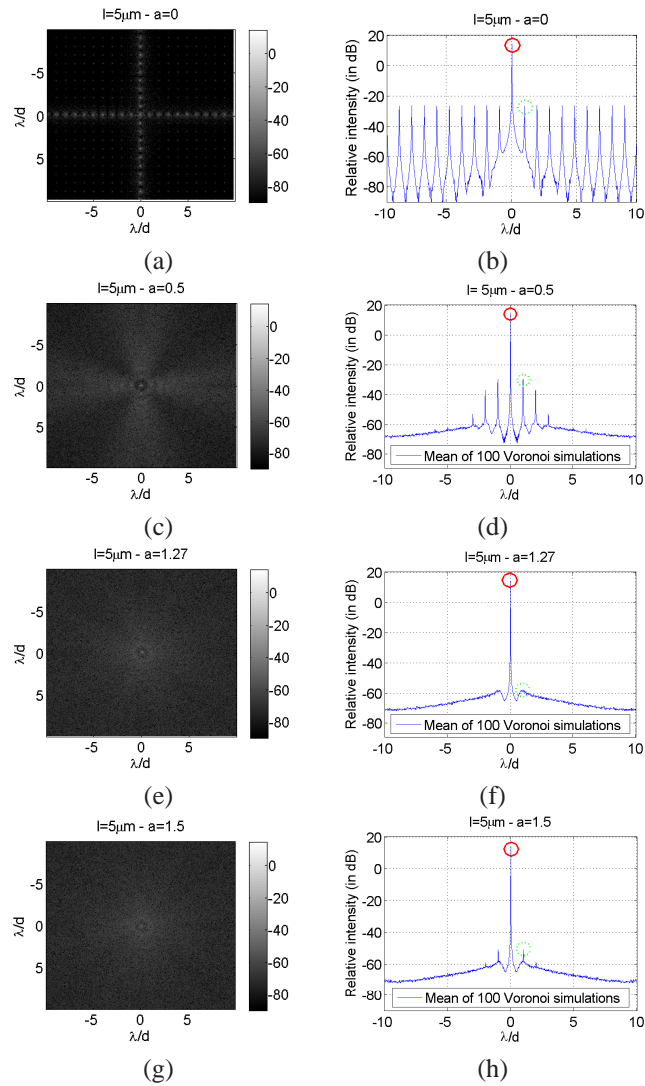
Fig. 3. Fraunhofer diffraction patterns of the components of Fig.2 (a, c, e, g) and their horizontal cross sections through the center (b, d, f, h) for $\lambda = 0.5\mu m$, $d = 100\mu m$, $l = 5\mu m$ and $R = 2mm$. The images as well as the cross-sections are shown in a logarithmic scale.
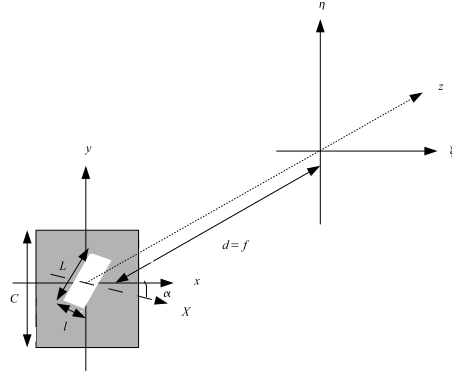
Fig. 4. Diffraction by a rectangular slit of width l, length L and orientation α

3. Model of the diffraction halo

We have seen in the previous section that when the Voronoi diagram is sufficiently distorted, the orientations of the walls are uniformly distributed over $[0, \pi]$ and the intensity distribution in the diffraction pattern looks like a halo. Our purpose in this section is to propose a heuristic model for the level and the angular variation of this halo. For that purpose, we will consider a set of N rectangular slits all included in a square aperture of side C. We assume that they are transparent (transmittance 1) whereas the rest of the square is absorbing (transmittance 0). We also assume that they have the same length L and width l but that their orientation angles α_k and their positions (x_k, y_k) are independent random variables. We introduce that object as a partial model of the Voronoi diagram, where the slits represent the walls separating the Voronoi pixels. Indeed, the opposite (opaque slits on a transparent background) would be a more accurate model, but as it is well known from Babinet's principle, the only difference would be the amplitude of the central peak. Moreover, we do not take into account the fact that in a Voronoi diagram, the lengths of the walls are different and that their orientations and their positions are not statistically independent since they are connected to form convex cells. As a result, it is expected that this model will represent the behavior of the halo but not of the higher order diffraction peaks.

As in the previous section, we will consider the diffracted intensity in the focal plane of a lens (see Fig. 4). Let us denote by $\theta_k = [\alpha_k, x_k, y_k]$ the vector of random variables that characterizes a rectangular slit and $f_{\theta_k}(x, y)$ its transmittance. One has :

$$f_{\theta_k}(x,y) = \text{rect}\left[\frac{\tilde{x}_k \sin\alpha_k - \tilde{y}_k \cos\alpha_k}{l}\right] \text{rect}\left[\frac{\tilde{x}_k \cos\alpha_k + \tilde{y}_k \sin\alpha_k}{L}\right] \tag{2}$$

where $\tilde{x}_k = x - x_k$, $\tilde{y}_k = y - y_k$ and the function rect(x) is equal to 1 when x belongs to $[-1/2, 1/2]$ and zero otherwise. As detailed in Appendix 5, and neglecting the fact that some of the slits may overlap, one can show that the average intensity $\langle I(\theta_{diff}) \rangle$ diffracted at angle θ_{diff} in the focal plane by the N slits is :

$$\langle I(\theta_{diff}) \rangle \simeq \frac{Nl^2 L^2}{\pi \lambda^2 f^2} \int_0^\pi \frac{\sin^2\left(\frac{\pi l}{\lambda} \tan\theta_{diff} \sin\varphi\right) \sin^2\left(\frac{\pi L}{\lambda} \tan\theta_{diff} \cos\varphi\right)}{\frac{\pi^4 l^2 L^2}{4\lambda^4} \tan^4\theta_{diff} \sin^2(2\varphi)} d\varphi \tag{3}$$

Because it relies on the incoherent superposition of all slit diffraction patterns, Eq. (3) is valid only outside the central peak $\theta_{diff} = 0$, where they all combine coherently. Indeed, for $\theta_{diff} =$
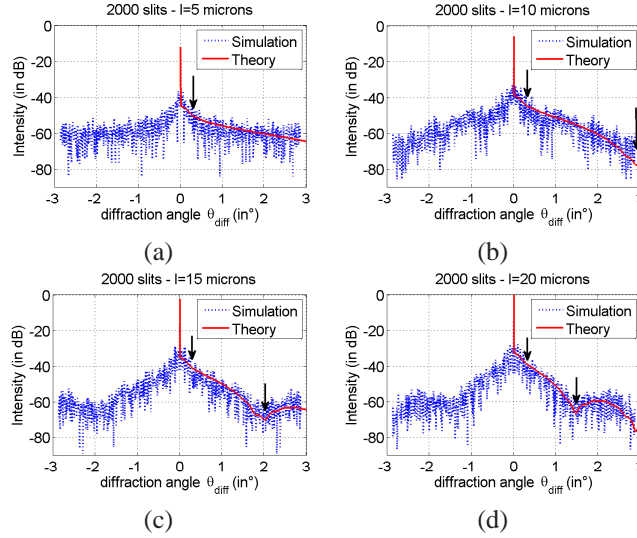
Fig. 5. Comparison, at $\lambda = 0.5\mu m$, of the diffracted intensity computed by the slits cloud simulation (dotted line) and the theoretical model given by Eq. (3) (solid line) for $N = 2000$ slits with random orientations and positions according to a uniform distribution over $[0, \pi]$ and $[-\frac{C}{2}, \frac{C}{2}]$. The length of all the slits is $L = 100\mu m$ and the width : (a) $l = 5\mu m$, (b) $l = 10\mu m$, (c) $l = 15\mu m$ and (d) $l = 20\mu m$.

0, as the transmittance of the slits is equal to 1 and the rest of the aperture has a transmittance equal to 0, one gets :

$$\langle I(0) \rangle \quad = \quad |\sum_k \tilde{f}_{\theta_k}(0,0)|^2 = \frac{1}{\lambda^2 f^2} |N\varepsilon|^2 \tag{4}$$

where ε is the surface of a rectangular slit.

In Fig. 5, we compare the result of Eq. (3) with the direct simulation of the intensity diffracted by a realization of a cloud of slits, which is given by the sum of the squared modulus of the Fourier transforms of all slits transmittances. The simulation was performed using a slit cloud model sampled at an interval of $5\mu m$. For each horizontal cross section represented in Fig. 5, the sampling by square numerical pixels increases the diffracted intensity by a factor corresponding to the squared modulus of their Fourier transform.

Two conclusions can be drawn. Firstly, Fig. 5 shows that the approximation we have made to obtain Eq. (3) [see Appendix 5, Eq. (19) and Eq. (21)] is valid. Secondly, we notice that the two curves in Fig. 5 feature slope breaks for the same diffraction angles. For example, in Fig. 5d, for slits with $l = 20\mu m$ and $L = 100\mu m$ and $\lambda = 0.5\mu m$, one gets slope breaks for $\theta_{diff1} \simeq 1.4^0$ and $\theta_{diff2} \simeq 0.29^0$. The positions of these slope breaks, indicated by arrows, correspond to the zeros of the two sinc functions that characterize each dimension of the slit [see Appendix 5, Eq. (18)]. They depend on the width l and the length L of the slits according to : $\theta_{diff1} \simeq m\lambda/l$ and $\theta_{diff2} \simeq m\lambda/L$, with m a non zero integer.

We now compare the result of Eq. (3) with the intensity distributions created by distorted Voronoi diagrams whose wall orientations are uniformly distributed over $[0, \pi]$. These Voronoi diagrams are generated in the same way as those in Fig. 2, with a deformation factor $a = \sqrt{2}$. Moreover, since Eq. (3) represents an ensemble mean over the possible wall orientations and positions, we average the intensities diffracted by 100 realizations of such Voronoi diagrams.
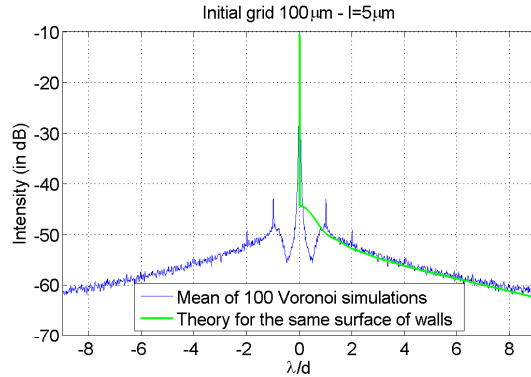
Fig. 6. Horizontal section of diffracted intensity pattern at $\lambda = 0.5\mu m$. Comparison between Voronoi simulations and the theoretical model given by Eq. (3). For all slits, $l = 5\mu m$. For the Voronoi simulations, the initial grid pitch is $d = 100\mu m$, $a = \sqrt{2}$ and $R = 2mm$. For Eq. (3), $L = 100\mu m$ for all the slits.

We compare on Fig. 6 the result of this simulation with the result of Eq. (3) for slits having width $l = 5\mu m$ and length $L = 100\mu m$. The number of slits has been chosen equal to $N = 2340$, so that the sum of the areas of the slits is equal to the average area of the walls generated in the Voronoi diagrams. We observe in Fig. 6 that the model leading to Eq. (3) gives us the behavior of the diffracted intensity of a Voronoi diagram as the diffraction angle varies.

The diffraction halo observed when the Voronoi diagram is sufficiently distorted is thus correctly modeled by the diffraction pattern of a cloud of slits of constant sizes, random positions and random orientations. Of course, this model cannot account for the residual diffraction peaks observed in Fig. 6 since the positions and the orientations of the slits are assumed uncorrelated, whereas it is obviously not the case in a connected Voronoi diagram. The next section will be devoted to the study of the behavior of these peaks.

4. Model for the higher order peaks

In this section, our objective is to explain the disappearance and reappearance of the higher order peaks when the deformation factor of the Voronoi diagram increases. We will first consider the simple case of a one-dimensional grid and demonstrate that there exists a value of the deformation factor for which the first order diffraction peak vanishes. We will then address the problem of two dimensional grids, whose theoretical study is not easily tractable. We will show by simulation that in this case, there is also a value of the deformation factor for which the first order diffraction peak disappears.

4.1. One-dimensional case

Let us consider a one dimensional structure composed of an infinite number of cells with the same length d separated by walls, as shown on Fig. 7. We assume that the transmittance of the walls is equal to 1 and that of the cells to 0, which means that the walls are transparent and the cells absorbing. The centres of each cell are then moved randomly so that their new positions are $x_k = kd + \alpha_k$, with α_k random variables that are independent and follow a uniform distribution on $[-\alpha/2, \alpha/2]$. After this movement, the new walls are in the middle of 2 successive new centres, at positions $x'_k = kd + \alpha'_k$ with $\alpha'_k = d/2 + (\alpha_k + \alpha_{k+1})/2$, as shown on Fig. 7. Our objective is to determine the diffraction pattern of this component at the focal plane of a
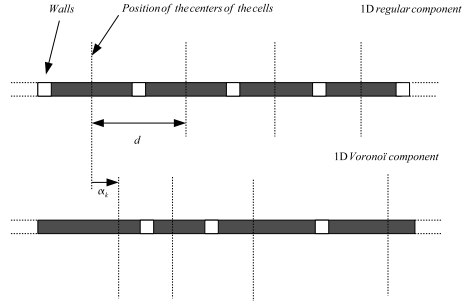
Fig. 7. 1D Voronoi component.

lens of focal f. For simplicity's sake, we assume that the walls are very thin. As a result, the transmittance of the component is proportional to a distorted Dirac comb :

$$D(x) \quad = \quad e \sum_{k=-\infty}^{\infty} \delta(x - kd - \alpha'_k) \tag{5}$$

where δ denotes the Dirac distribution and e is the width of the walls. The amplitude $U(v)$ of the field in the focal plane of the lens is proportional to the Fourier transform $\tilde{D}(v)$ of this transmittance, with $v = \xi/\lambda f$ and ξ the coordinate of a point in the focal plane. The expected value of this amplitude is equal to :

$$\langle U(v) \rangle = e \left\langle \exp(-2\iota\pi v\alpha'_k) \right\rangle \sum_{k=-\infty}^{\infty} \exp(-2\iota\pi vkd) \tag{6}$$

where the symbol $<>$ denotes ensemble averaging over the realizations of the random variables α'_k. Using the following well known identity relative to the Dirac comb :

$$\sum_{k=-\infty}^{\infty} \exp(-2\iota\pi vkd) \quad = \quad \frac{1}{d} \sum_{k=-\infty}^{\infty} \delta\left(v - \frac{k}{d}\right) \tag{7}$$

and using the fact that the characteristic function of a random variable X is the Fourier transform of its probability density function $\tilde{P}_X(v) = \langle \exp(-2\iota\pi vX) \rangle$, Eq. (6) becomes :

$$\langle U(v) \rangle \quad = \quad \frac{e}{d} \sum_{k=-\infty}^{\infty} \tilde{P}_{\alpha'}\left(\frac{k}{d}\right) \delta\left(v - \frac{k}{d}\right) \tag{8}$$

where we have taken into account that the random variables α'_k are identically distributed and thus have the same characteristic function $\tilde{P}_{\alpha'}$. Since the random variables α_k are uniform, their characteristic function is $\tilde{P}_\alpha(v) = \text{sinc}(v\alpha)$ with sinc(x) $= \sin(\pi x)/\pi x$. Moreover, since $\alpha'_k = d/2 + (\alpha_k + \alpha_{k+1})/2$, we obtain :

$$\tilde{P}_{\alpha'}(v) \quad = \quad \frac{1}{2} \exp(-\iota\pi vd) \left[\tilde{P}_\alpha\left(\frac{v}{2}\right)\right]^2 = \frac{1}{2} \exp(-\iota\pi vd) \left[\text{sinc}\left(\frac{v\alpha}{2}\right)\right]^2 \tag{9}$$

As a result, Eq. (8) becomes :

$$\langle U(v) \rangle \quad = \quad \frac{e}{2d} \sum_{k=-\infty}^{\infty} \exp(-\iota k\pi) \left[\text{sinc}\left(\frac{ka}{2}\right)\right]^2 \delta\left(v - \frac{k}{d}\right) \tag{10}$$
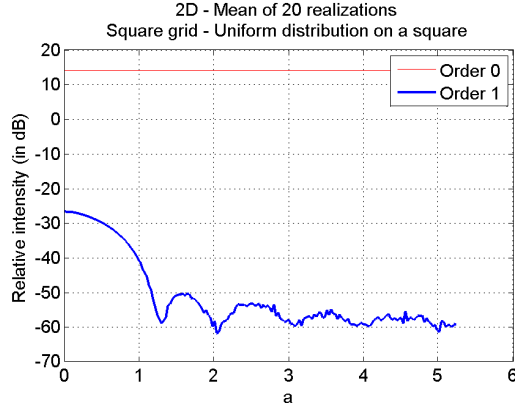
Fig. 8. Average of the relative intensities on 20 realizations of 2D Voronoi components at $\lambda = 0.5\mu m$. The initial grid pitch is $d = 100\mu m$, the length of the wall is $e = 5\mu m$, and $R = 2mm$.

with the one-dimensional deformation factor $a = \alpha/d$ identical to Eq. (1). The kth order of the intensity pattern is thus equal to :

$$O_k = \left|\left\langle U\left(\frac{k}{d}\right)\right\rangle\right|^2 = \frac{e^2}{4d^2}\left[\text{sinc}\left(\frac{ka}{2}\right)\right]^4 \tag{11}$$

We notice that the intensity O_1 of the first order peak is equal to zero for $a = 2l$ with l integer and $l \geq 1$. The first annulation is given by $\alpha = 2d$, that is, when the range of allowed displacement α is the double of the period d of the initial grid.

4.2. Two-dimensional case

In the 1D case, we have been able to analytically explain the disappearance and reappearance of the diffraction orders according to the deformation parameter a. For 2D Voronoi diagrams, the theoretical approach is much more involved. Therefore, in this section, we will only perform simulations and analyze their results. We will study the evolution of the first order as a function of the parameter a for 2D Voronoi components generated as in Section 2 (see Fig. 2).

We plot on Fig. 8 the evolution of the relative intensity of the order 1 as a function of the parameter a. If we denote (ξ, η) the coordinates of a point in the focal plane, the relative intensity $E(\xi, \eta)$ is defined by $E(\xi, \eta) = I(\xi, \eta)/I_0$, where $I(\xi, \eta)$ is the intensity diffracted by the component at the point (ξ, η), and I_0 is the intensity in the order 0 when the transmittance is equal to 1 everywhere in the circular pupil of surface A, that is, $I_0 = A^2/\lambda^2 f^2$.

The curve in Fig. 8 has some properties in common with Eq. (11). It has several local minima : the first one is situated at $a = 1.27$, and it seems that the others are situated closed to $a = l$ with l integer and $l \geq 2$, which is similar to the 1D case. This result is consistent with what is observed in Fig. 3f, where we can verify that for $a = 1.27$, we have a total annulation of the first order peak. It is also consistent with the fact that for $a > 1.27$, the first order peak reappears (Fig. 3h).

In conclusion, it is possible to cancel the main unwanted diffraction peaks and essentially obtain a pure diffraction halo by a suitable choice of parameters in our simple technique of generation of Voronoi diagrams. Starting with an initial square-shaped grid and using a uniform probability density function for the displacement of the grid centres may seem arbitrary.

We have performed tests on various initial grid shapes (square and hexagonal) and different probability density functions (a uniform distribution on a square of side $[-\alpha/2, \alpha/2]$, a uniform distribution on a disk of radius $r = \alpha/2$ and an isotropic gaussian distribution with a standard deviation α) to displace the grid centres.

For all these deformation statistics, there is a specific value of the deformation parameter $a = \alpha/d$, which is in general different from 1.27, that leads to the disappearance of the higher order peaks. The Voronoi grids obtained for these parameter values have the same properties : uniform orientation of the walls and identical shape and level of the halo. We have not yet been able to analytically account for that particular set of values of the parameter a in the 2D case as we did in 1D, but we think that it is an interesting subject for further investigation.

The method described in this paper is intended to reduce the diffraction peaks and to replace them by a halo. This is beneficial when SLMs are used for imaging purposes, such as in active lenses, when the point spread function includes the order 0 as well as the higher orders. For example when imaging bright point-like objects on a dark background the effects of the diffraction peaks can be very annoying. Of course, there are other applications like optical tweezers where SLMs are only used to shape the order 0, and where higher order peaks may not be annoying. Although our method does not significantly increase the background noise around the order 0, it does not serve a useful purpose in such applications.

5. Conclusion

We have proposed a simple way to design SLM grid structures that minimize the diffraction peaks due to the periodic arrangement of cell walls. We have demonstrated that by starting from a regular square-shaped grid and deforming it with the technique of Voronoi diagrams, it is possible to completely cancel the main unwanted diffraction peaks for specific values of the deformation parameter. For these values, the diffraction pattern only consists of an order 0 and of a slowly varying diffusion halo, which is much less annoying for the observer than the diffraction peaks produced by a regular grid. We have shown that the halo can be ascribed to the diffraction by randomly oriented and positioned segments. Tests performed on various grid shapes and various strategies for the cell deformations lead to the same conclusions.

This work has many perspectives. In particular, we have assumed in this paper that all the cells have the same phase. It would be interesting to study the case where the SLM implements a phase function so that the phase value in each cell is different.

Appendix: Intensity diffracted by a random cloud of slits

We call $f_{\theta_k}(x, y)$ the transmittance of one rectangular slit. According to Fig. 4, for a given position (x_k, y_k) and a given orientation α_k of a slit, the transmittance is given by Eq. (2). If we now consider N slits, the output field of the component in the lens plane can be expressed as :

$$A(x, y) = \sum_{k=1}^{N} f_{\theta_k}(x, y) \tag{12}$$

With a good approximation, the diffracted intensity in the focal plane of a lens of focal length f is given by :

$$I(\xi, \eta) = \frac{1}{\lambda^2 f^2} \sum_k \left| \tilde{f}_{\theta_k}(\xi, \eta) \right|^2 + \frac{1}{\lambda^2 f^2} \sum_k \sum_{l, k \neq l} \tilde{f}_{\theta_k}(\xi, \eta) \tilde{f}_{\theta_l}^*(\xi, \eta) \tag{13}$$

where :

$$\tilde{f}_{\theta_k}(\xi, \eta) = lL \text{sinc}\left[\frac{l}{\lambda f}(\xi \sin \alpha_k - \eta \cos \alpha_k)\right] \text{sinc}\left[\frac{L}{\lambda f}(\xi \cos \alpha_k + \eta \sin \alpha_k)\right]$$
$$\exp\left[-\frac{2\iota\pi}{\lambda f}(\xi x_k + \eta y_k)\right] \tag{14}$$

with the function $\text{sinc}(x) = \sin(\pi x)/\pi x$. Let us consider the ensemble mean of each term of Eq. (13) over the realizations of x_k, y_k, α_k. Let $P_x(x_k)$, $P_y(y_k)$ and $P_\alpha(\alpha_k)$ be the probability density functions of the random variables x_k, y_k and α_k with $k \in [1, N]$. We assume that the 3N random variables, x_k, y_k and α_k are independent and that $P_x(x_k)$ and $P_y(y_k)$ are uniform distributions on $[-C/2, C/2]$. Thus, the ensemble mean of the first term of Eq. (13) is equal to :

$$\left\langle \frac{1}{\lambda^2 f^2} \sum_k |\tilde{f}_{\theta_k}(\xi, \eta)|^2 \right\rangle = \frac{N}{\lambda^2 f^2} \int_0^\pi |\tilde{f}_{\theta_k}(\xi, \eta)|^2 P_\alpha(\alpha_k) d\alpha_k \tag{15}$$

According to Eq. (14), one has in cartesian coordinates:

$$|\tilde{f}_{\theta_k}(\xi, \eta)|^2 = l^2 L^2 \text{sinc}^2\left[\frac{l(\xi \sin \alpha_k - \eta \cos \alpha_k)}{\lambda f}\right] \text{sinc}^2\left[\frac{L(\xi \cos \alpha_k + \eta \sin \alpha_k)}{\lambda f}\right] \tag{16}$$

Let us express this equation in polar coordinates (ρ, ψ) : $\xi = \rho \cos \psi$ and $\eta = \rho \sin \psi$. One has :

$$|\tilde{f}_{\theta_k}(\rho, \psi)|^2 = l^2 L^2 \text{sinc}^2\left[\frac{l}{\lambda f}(\rho \sin(\alpha_k - \psi))\right] \text{sinc}^2\left[\frac{L}{\lambda f}(\rho \cos(\alpha_k - \psi))\right] \tag{17}$$

Denoting, $\tan \theta_{diff} = \rho/f$ and $\varphi = \alpha_k - \psi$, one has :

$$|\tilde{f}_{\theta_k}(\theta_{diff}, \varphi)|^2 = l^2 L^2 \text{sinc}^2\left[\frac{l}{\lambda}(\tan \theta_{diff} \sin \varphi)\right] \text{sinc}^2\left[\frac{L}{\lambda}(\tan \theta_{diff} \cos \varphi)\right] \tag{18}$$

Since we assume that the orientation variable α_k of the rectangular slits is uniformly distributed over $[0, \pi]$: $P_\alpha(\alpha_k) = P_\alpha(\varphi + \psi) = \frac{1}{\pi}$ over $[0, \pi]$ and 0 outside, one gets :

$$\left\langle \frac{1}{\lambda^2 f^2} \sum_k |\tilde{f}_{\theta_k}(\xi, \eta)|^2 \right\rangle \simeq \frac{N}{\lambda^2 f^2 \pi} \int_0^\pi |\tilde{f}_{\theta_k}(\theta_{diff}, \varphi)|^2 d\varphi$$
$$\simeq \frac{Nl^2 L^2}{\pi \lambda^2 f^2} \int_0^\pi \frac{\sin^2(\frac{\pi l}{\lambda} \tan \theta_{diff} \sin \varphi) \sin^2(\frac{\pi L}{\lambda} \tan \theta_{diff} \cos \varphi)}{\frac{\pi^4 l^2 L^2}{4\lambda^4} \tan^4 \theta_{diff} \sin^2(2\varphi)} d\varphi \tag{19}$$

For the ensemble mean of the second term of Eq. (13), since we assume that the orientation and position variables are independent, one has :

$$\left\langle \sum_k \sum_{l, k \neq l} \tilde{f}_{\theta_k}(\xi, \eta) \tilde{f}_{\theta_l}^*(\xi, \eta) \right\rangle = N(N-1) \int \int \int \int \int \int \tilde{f}_{\theta_k}(\xi, \eta) \tilde{f}_{\theta_l}^*(\xi, \eta)$$
$$P_\alpha(\alpha_k) P_x(x_k) P_y(y_k) P_\alpha(\alpha_l) P_x(x_l) P_y(y_l) d\alpha_k dx_k dy_k d\alpha_l dx_l dy_l \tag{20}$$

According to Eq. (14) and the fact that $P_x(x_k)$, $P_x(x_l)$, $P_y(y_k)$ and $P_y(y_l)$ are uniform distributions on $[-C/2, C/2]$, it reduces to :

$$\left\langle \sum_k \sum_{l, k \neq l} \tilde{f}_{\theta_k}(\xi, \eta) \tilde{f}_{\theta_l}^*(\xi, \eta) \right\rangle = N(N-1) L^2 l^2 I_a^2(\xi, \eta) \text{sinc}^2\left(\frac{\xi C}{\lambda f}\right) \text{sinc}^2\left(\frac{\eta C}{\lambda f}\right) \tag{21}$$

with :

$$I_a(\xi, \eta) = \int_0^\pi \mathrm{sinc}\left[\frac{l}{\lambda f}(\xi \sin \alpha_k - \eta \cos \alpha_k)\right]$$
$$\mathrm{sinc}\left[\frac{L}{\lambda f}(\xi \cos \alpha_k + \eta \sin \alpha_k)\right] P_\alpha(\alpha_k) d\alpha_k \qquad (22)$$

Equation (21) is equal to 0 outside the center of the Airy function of the aperture, that is, for $\xi \gg \lambda f/C$ and for $\eta \gg \lambda f/C$. These considerations prove that the diffracted intensity in the focal plane is given by Eq. (19) for $(\xi, \eta) \neq (0,0)$. To conclude, Eq. (19) is always a valid expression of the average scattered light intensity diffracted in the lens focal plane by the slits cloud, except in a neighborhood of order $1/C$ near the origin $\theta_{diff} = 0$. For $\theta_{diff} = 0$, as the transmittance of the slits is equal to 1 and the rest of the square has a transmittance equal to 0, one gets :

$$\langle I(0) \rangle \quad = \quad |\sum_k \tilde{f}_{\theta_k}(0,0)|^2 = \frac{1}{\lambda^2 f^2}|N\varepsilon|^2 \qquad (23)$$

where ε is the surface of a rectangular slit. So, we will numerically estimate the integral of Eq. (19) and we will determine separately the order 0.

Acknowledgments